CO_2 气体保护焊电弧温度场和流场建模与分析

夏胜全，　区智明，　孙晓明
（清华大学 先进成形制造教育部重点实验室，北京　100084）

夏胜全

摘　要： 建立了 CO_2 气体保护焊焊接电弧三维瞬态模型，通过采集实际 CO_2 气体保护焊瞬变电流数据，运用磁流体动力学（magneto hydrodynamics，MHD）等基本理论，结合 ANSYS 的多物理场耦合功能，模拟出了 CO_2 气体保护焊焊接电弧的电场电流密度、磁场电磁力、温度和速度场的分布. 电弧温度场分布模拟结果和文献中的试验数据基本一致. 同时通过计算系统的流体雷诺数和马赫数对该模型中的流体层流假设和不可压缩假设的合理性进行了验证. 该数学模型可为控制 CO_2 气体保护焊焊接电弧提供理论指导，也为进一步分析 CO_2 气体保护焊电弧的动态过程打下了基础.

关键词： 焊接电弧；数值建模；多物理场耦合
中图分类号： TG444　　**文献标识码：** A　　**文章编号：** 0253－360X(2013)11－0097－04

0　序　　言

随着计算机硬件的高速发展，采用数值计算对焊接电弧的模拟越来越多. 焊接电弧涉及电场、磁场和温度场等比较复杂的物理过程，通过试验对焊接电弧的传热和流体流动过程检测费时、费力或无法完成. 通过数值模拟对电弧的流场和温度场进行分析，具有指导价值和经济价值. 一方面，大多文献对电弧的分析均为稳态或准稳态[1-7]，瞬变电流的分析较少. 另一方面，国内外文献分析的气体多为氩气[1-5]，纯 CO_2 电弧研究较少. 选取生产中应用较广的 CO_2 气体保护焊为分析对象，采集焊接电流数据，建立电弧温度场和流场的数值模型，为控制 CO_2 气体保护焊焊接电弧提供理论指导，为后续分析打下基础.

1　数学模型

1.1　简化条件及计算域

采用纯 CO_2 为保护气体，为简化计算，作如下假设：(1) 电弧处于局部热动态平衡（LTE）；(2) 辐射的重新吸收可以忽略不计；(3) 电弧是连续的和对称的；(4) 流动处于不可压缩层流状态；(5) 粘性效应导致的热损失忽略不计. 为减小计算量，建立 1/4 模型. 计算域如图 1 所示.

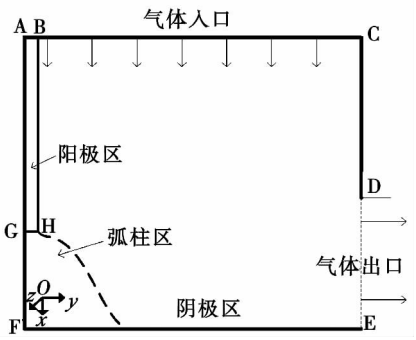

图 1　电弧计算域示意图
Fig. 1　Schematic of arc calculation domain

1.2　控制方程

电弧属流体，遵循流体三大方程.

(1) 质量守恒方程（连续性方程），即

$$\frac{\partial \rho}{\partial t}+\rho\,\nabla v_{\mathrm{s}}=0 \tag{1}$$

(2) 动量守恒方程（N-S 方程），即

$$\rho\frac{\mathrm{d}v_{\mathrm{s}}}{\mathrm{d}t}=-\nabla p+\mu\,\nabla^2 v_{\mathrm{s}}+\boldsymbol{J}\cdot\boldsymbol{B} \tag{2}$$

(3) 能量守恒方程，即

$$\rho\frac{\mathrm{d}H}{\mathrm{d}t}=\frac{\mathrm{d}p}{\mathrm{d}t}+\nabla\left(\frac{k}{c_{\mathrm{p}}}\nabla H\right)+\Phi-S_{\mathrm{r}}+\frac{\boldsymbol{J}^2}{\gamma} \tag{3}$$

式中：ρ 为等离子体密度；v_{s} 为速度；p 为压力；μ 为粘性系数；H 为焓值；c_{p} 为定压比热容；k 为热导率；S_{r} 为辐射流密度；Φ 为耗散功率；$\boldsymbol{B}$ 为磁感应强度；γ 为电导率；$\boldsymbol{J}$ 为电流密度；t 为时间；∇ 为散度运算算子.

收稿日期：2012－07－23

电弧形成电磁场遵循 Maxwell 方程组，电流连续性方程为

$$\nabla \boldsymbol{J} = 0 \tag{4}$$

欧姆定律为

$$\boldsymbol{J} = \sigma_e \boldsymbol{E} \tag{5}$$

安培环流定律为

$$\nabla \boldsymbol{B} = \mu_0 \boldsymbol{J} \tag{6}$$

式中：$\boldsymbol{E}$，σ_e，μ_0 分别为电场矢量、电导率、真空磁导率.

1.3 边界条件

BC 为气体入口，给定入口速度；CD 为喷嘴内壁，DE 为气体出口.

1.3.1 电场边界条件

焊丝上施加电流和电压载荷，阴极电势为 0，其它面电势垂直壁面的导数为 0.

CO_2 在温度低于 5 000 K 时，电导率很低，因此初始计算时，设定弧柱区初始温度为 7 000 K，让其处于导电状态.

1.3.2 磁场边界条件

电弧对称面加磁感应强度垂直边界条件；其它面假定无限远处磁感应强度为 0.

1.3.3 流场边界条件

上表面为流体入口，柱面上半部为固定壁面（喷嘴内壁），下部为压力出口，其余为壁面；采用负体积热源方式施加 CO_2 辐射损失.

2 计算过程

2.1 有限元模型

采用变步长映射网格，焊丝及电弧区域网格加密，网格划分如图 2 所示.

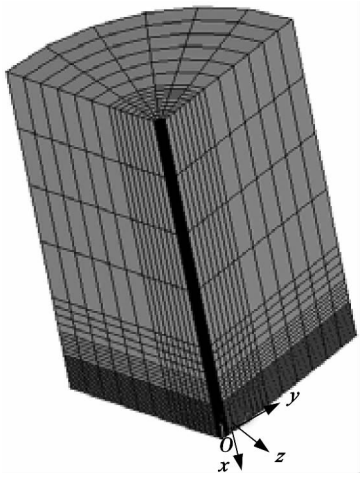

图 2 变步长映射网格划分

Fig. 2 Variable step-size mapping mesh

2.2 计算流程

采集试验电流数据，截取燃弧段的离散电流点. 单个电流点计算流程描述为先计算电场，求出电流密度分布，代入磁场计算，得到生热率和电磁力，代入流场进行温度场和速度场计算，之后再将计算的温度场代入电场计算，反复迭代，直至各场收敛. 再将当前温度场和流场作为初场，计算下一电流点，直至全部电流点计算完成. CO_2 电阻率等物理性质随温度变化，具体内容见参考文献 [7－9].

3 计算结果及分析

CO_2 短路过渡焊典型电流波形如图 3 所示.

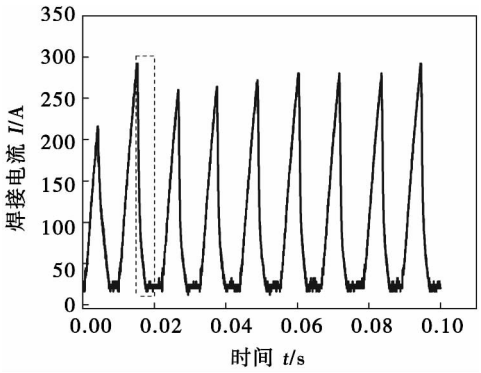

图 3 焊接电流波形

Fig. 3 Current waveform in welding

短路时电弧熄灭，因此截取其中一个典型周期的燃弧阶段电流数据（图 3 中虚框）. 采样频率为 10 MHz，气体流量为 15 L/min，弧长为 3 mm，焊丝直径为 1.2 mm，喷嘴直径为 30 mm.

3.1 电弧温度场

模拟发现，1 ms 左右电弧趋于稳定，为观察电弧瞬态过程，查看约 0.5 ms 数据，典型 CO_2 气体保护焊电弧温度场，如燃弧后0.49 ms温度场如图4

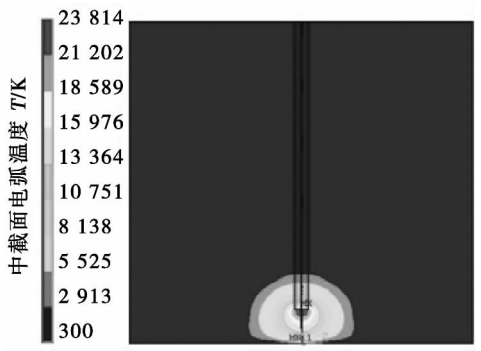

图 4 电弧温度场

Fig. 4 Temperature distribution of arc

所示.

为方便查看，给出 1/2 模型. 由图 4 中可看出，处于焊丝端部电弧温度最高，靠近阴极附近，由于钢板熔化吸热等效应，电弧温度场有所收缩.

电弧温度场常用的测量方法为光谱法，文中模拟的电弧为瞬变的 CO_2 电弧，运用光谱法测量其温度场存在较大的难点，由于光谱仪存在最短曝光时间以及计算转换时间等，使其测量瞬变电弧几乎无法实现. 其它测量方法实现起来也比较困难. 鉴于稳定的氩电弧温度场测量已经有成熟的试验数据，为对温度场进行验证，简单修改模型参数，弧长改为 10 mm，焊接电流固定为 120 A，保护气体变为氩气，和文献 [1] 试验结果对比如图 5 所示.

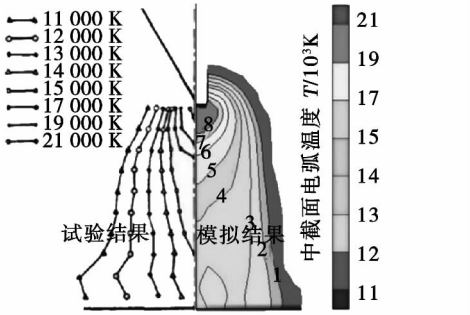

图 5　试验和模拟结果

Fig. 5　Results of experiment and simulation

由图 5 中可以看出，该模拟结果和试验结果基本一致，从而证明该模型的正确性和合理性.

图 6 给出了 CO_2 气体保护焊电流和电弧最高温度关系曲线.

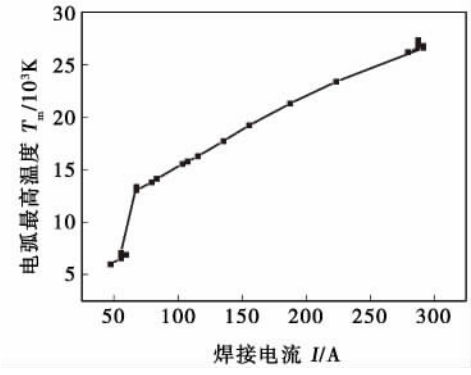

图 6　CO_2 电弧最高温度和瞬时电流关系曲线

Fig. 6　Relationship between maximum temperature and instantaneous current of CO_2 arc

随焊接电流减小，电弧热效应降低，最高温度下降，当电弧温度不足以满足热电离和电导性要求时，电弧熄灭.

3.2　电流密度分布

图 7 给出了燃弧后 0.49 ms 电流密度分布. 由图 7 可观察到，焊丝下端附近，电流密度最大，导电区域主要集中在电弧下方，呈发射状流向阴极，其它区域温度较低，气体无电离，处于不导电状态，同一电弧截面上，随径向半径增大，电流密度减小.

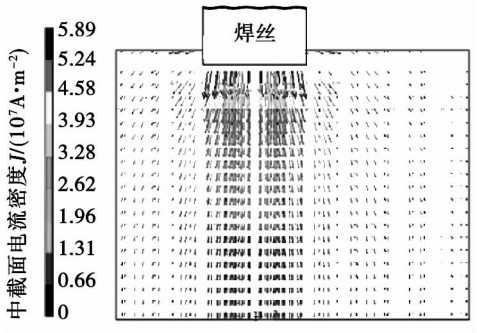

图 7　电流密度分布(t = 0.49 ms)

Fig. 7　Distribution of arc current density

3.3　电磁力分布

图 8 给出了 1/4 模型放大焊丝附近区域结果.

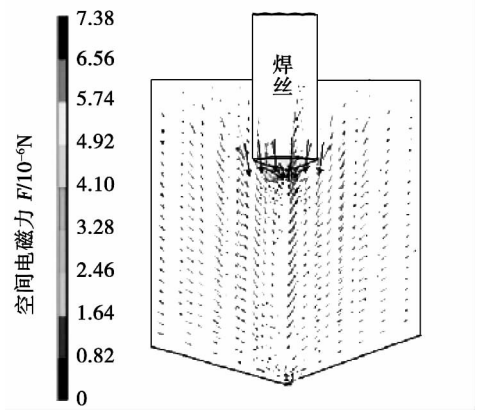

图 8　电磁力分布(t = 0.49 ms)

Fig. 8　Distribution of electromagnetic force

处于焊丝下方附近，由于电流密度较大，等离子流速较大，使得电弧中的带电粒子所受洛伦兹力较大；电磁场引起的电弧收缩效应也较明显.

3.4　电弧流场分布

燃弧后 0.49 ms 焊丝下端附近的局部流场分布放大如图 9 所示.

由流场速度分布可以看到，靠近焊丝附近的流速较大，处于阴极附近，流速趋于 0.

3.4.1　流体层流假设的验证

当流体雷诺数大于 2 100 时，流体开始向湍流

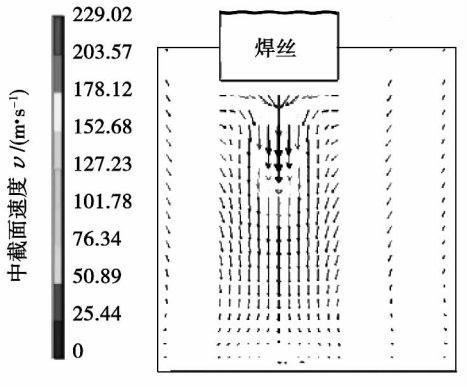

图 9 流场分布(t =0.49 ms)

Fig. 9 Distribution of fluid field

转变. 雷诺数计算式为

$$R_e = \frac{\rho v' r}{\eta} \tag{7}$$

式中: v' 为特征速度; r 为物体特征长度; η 为流体动态粘度. 将模拟的最高温度下对应的密度和粘度作流体密度和粘度,将最大速度作特征速度代入,得各时刻近似雷诺数如图 10 所示.

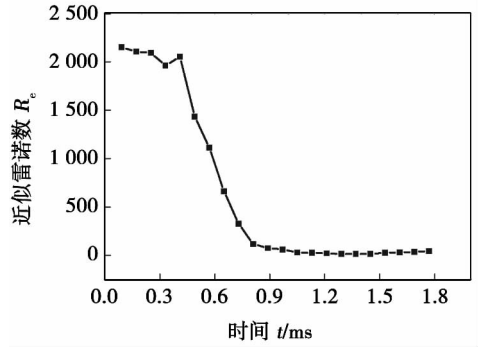

图 10 近似雷洛数变化曲线

Fig. 10 Change curve of approximate reynolds number

当 R_e 小于 2 100 时,视为层流. 由图 10 可知,该流体雷诺数基本小于 2 100,假设为层流是合适的.

3.4.2 流体压缩假设的验证

马赫数 M 为流场中某点速度与该处音速之比. 通过计算可以得到各时刻最大马赫数 M_{max},其变化趋势和图 10 中雷诺数变化趋势类似,即随着时间增大,最大马赫数减小. 马赫数大于 0.3 时,认为气体可压缩. 而流场中最大马赫数为 0.11,可不考虑流体的压缩性能.

4 结 论

(1) 采用大型通用计算软件 ANSYS,对常用 CO_2 气体保护焊电弧建立了三维瞬态模型.

(2) 采集实际 CO_2 气体保护焊焊接电流数据,代入该数学模型,给出了焊接电弧的电流密度分布、电磁力分布、温度和速度分布.

(3) 通过模拟数据检验模型采用不可压缩层流模型的假设是合适的.

参考文献:

[1] Hsu K C, Etemadi K, Pfender E. Study of the free-burning high-intensity argon arc [J]. Journal of Applied Physics, 1983, 54(3): 1293 - 1301.

[2] 雷玉成, 李彩辉, 郁雯霞, 等. 氮氩气体保护 TIG 焊接电弧数值分析 [J]. 焊接学报, 2006, 27(11): 25 - 28.
Lei Yucheng, Li Caihui, Yu Wenxia, *et al*. Numerical analysis of N_2-Ar protecting tungsten inert gas welding arc [J]. Transactions of the China Welding Institution, 2006, 27(11): 25 - 28.

[3] 殷凤良, 胡绳荪, 郑振太, 等. 等离子弧焊电弧的数值模拟 [J]. 焊接学报, 2006, 27(8): 51 - 54.
Yin Fengliang, Hu Shengsun, Zheng Zhentai, *et al*. Numerical analysis of arc in plasma arc welding [J]. Transactions of the China Welding Institution, 2006, 27(8): 51 - 54.

[4] Schnick M, Dreher M, Zschetzsche J, *et al*. Visualization and optimization of shielding gas flows in arc welding [J]. Welding in the World, 2012, 56(1): 54 - 61.

[5] 成满庆, 安艳丽, 杜华云, 等. 电流参数变化对电弧温度场和速度场的影响 [J]. 焊接学报, 2010, 31(4): 33 - 37.
Cheng Manqing, An Yanli, Du Huayun, *et al*. Effect of current changes on velocity and temperature profiles of GTAW arc [J]. Transactions of the China Welding Institution, 2010, 31(4): 33 - 37.

[6] Choquet I. Numerical simulation of Ar-x% CO_2 shield gas and its effect on an electric welding arc [C] //IIW Commission XII/SG 212 Intermediate Meeting. Sweden, Trollhättan, 2011: 1 - 12.

[7] Schnick M, Wilhelm G, Lohse M, *et al*. Three-dimensional modeling of arc behavior and gas shield quality [J]. Journal of D: Applied Physics, 2011, 44(18): 1 - 25.

[8] André P, Aubreton J, Clain S, *et al*. Transport coefficients in thermal plasma. Applications to mars and titan atmospheres [J]. The European Physical Journal D, 2010, 57(2): 227 - 234.

[9] Cressault Y, Connord V, Hingana H, *et al*. Transport properties of CF_3I thermal plasmas mixed with CO_2, air or N_2 as an alternative to SF_6 plasmas in high-voltage circuit breakers [J]. Journal of Applied Physics, 2011, 44: 4 - 18.

作者简介: 夏胜全,男,1982 年出生,博士研究生. 主要从事焊接过程控制和模拟. 发表论文 1 篇. Email: xiashengquan2001@163.com

welded by double beam laser welding was developed based on birth-death control by the temperature of each element. In the method, an element was killed or activated according to its temperature during welding. The welding deformation obtained by two different computational methods were compared, one using the birth-death control method, and the other not. Except the above difference, material, geometry, boundary and initial conditions were identical for the two computational methods. The results showed that, whether using the birth-death control or not, which had an important influence on the computational results of deformation of T joint welded by double beam laser welding, and the reason was analyzed.

Key words: T joint; double beam laser welding; welding deformation

Numerical simulation of temperature and flow field of CO_2 gas shielded arc XIA Shengquan, OU Zhiming, SUN Xiaoming (Key Laboratory for Advanced Materials Processing Technology, Tsinghua University, Beijing 100084, China). pp 97 – 100

Abstract: A transient three-dimensional model of welding arc in CO_2 gas shielded arc welding was founded. With the experimental data of transient welding current, the basic theory of magneto hydrodynamics (MHD) and the coupling of multi-physics function of ANSYS, the distribution of the current density in electric field, the electromagnetic force in magnetic field, the temperature and velocity in the flow field were simulated. The simulation result for arc temperature filed is basically identical with the experimental data in the reference. In addition, the laminar hypothesis and incompressible assumption in the model were verified by computing the Reynolds number and Mach number. The numerical model can provide theoretical guidance with the controlling of welding arc in the CO_2 gas shielded arc welding, and it also lays a foundation for the further study on the analysis of transient CO_2 arc.

Key words: welding arc; numerical modeling; multi-field coupling

Interfacial IMC evolution in micron Sn-Ag-Cu soldered joint during thermal aging TIAN Ye[1,2], WU Yiping[2], AN Bing[2], LONG Danfeng[3] (1. School of Mechanical and Electrical Engineering, Henan University of Technology, Zhengzhou 450001, China; 2. School of Materials Science and Engineering, Huazhong University of Science and Technology, Wuhan 430074, China; 3. Department of Precision Instruments and Mechanology, Tsinghua University, Beijing 100084, China). pp 101 – 104

Abstract: The interfacial intermetallic compound (IMC) evolution in micro-soldered joints in thermal aging process of flip-chip assemblies was investigated. The results show that all $(Ni,Cu)_3Sn_4$ on the Ni pad interface are transformed into $(Cu,Ni)_6Sn_5$ after 300 h for thermal aging due to the effect of Cu atoms diffused from the Cu pad interface on the $(Ni,Cu)_3Sn_4$. On the Cu pad interface, a thin layer of Cu_3Sn forms on the interface between the Cu pad and $(Cu,Ni)_6Sn_5$ after 100 h for aging, however in the subsequent thermal aging, Cu_3Sn experiences little growth because of the limitation effect of Ni on its growth. The growth rate of $(Cu,Ni)_6Sn_5$ on the both pad interfaces are fast before 100 h, and after 100 h, it become slower and slower. Furthermore, as the aging time increases, the interface of $(Cu,Ni)_6Sn_5$ grain inclines to be flat.

Key words: lead-free solder; intermetallic compound; flip chip assembly; interfacial reaction; thermal aging

Research on A-MAG welding of weathering resistant steel LU Hao[1], XING Liwei[2], CHEN Dajun[3] (1. Technical Engineering Department, CSR Qingdao Sifang Co., Ltd., Qingdao 266111, China; 2. Technology Center, CSR Qingdao Sifang Co., Ltd., Qingdao 266111, China; 3. Harbin Welding Training Institute, Harbin 150046, China). pp 105 – 108

Abstract: A-MAG welding was proposed to obtain the welded joints with high quality. The experiment results show that A-MAG weld appearance, internal quality of welded joint and the welding operation performance are very well. Experiments also show that the A-MAG welding can improve weld penetration, which is compared with MAG welding under the same heat input. The tensile strength and bending strength of A-MAG welded joint are not reduced, while impact strength is improved, especially in the HAZ. Dimples size in fracture appearance of A-MAG welded joint is finer. It is showed that the active MAG welding can improve the welding quality and weld penetration of weathering resistant steel, which is applicable in engineering application.

Key words: A-MAG welding; weathering resistant steel; high speed train

Grain types and composition distribution of agglomerated flux with high slag detachability XU Guoliang[1], ZHENG Zhentai[1], LIU Pengfei[2], ZHANG Lisheng[1], WANG Tao[1] (1. School of Materials Science and Engineering, Hebei University of Technology, Tianjin 300132, China; 2. Luo Yang Institute of Ship Materials, Luoyang 471023, China). pp 109 – 112

Abstract: In order to enhance slag detachability of agglomerated flux for low-alloy steel in root bead, uniform design method was used to optimize slag systems for MgO-Al_2O_3-CaO with high basicity and slag detachability test. Then scanning electron microscopy (SEM), energy dispersive x-ray analysis (EDAX) and X-ray diffraction (XRD) were used to analyze the microstructure, compositions and phase of slag. The results show that the No. 10 slag with higher detachability is mainly made of compound rock phases, whose main elements are Zr, Mg, Ca, Al and Si. Since the element content is different in slag microzone, it can form snowflake grain with Zr, cross grain with Mg, and dentrite with Ca. Dentrite with Ca and snowflake grain with Zr can hinder the growth of cross grain with Mg. In addition, Zr has a role in refining cross grain with Mg. So the increase of the contents of marble and zircon sand in flux can change the continuity and direction of cross grain with Mg in slag. It will be a valid way to improve slag detachability.

Key words: agglomerated flux; microstructure; composition distribution; slag detachability